

Two-Dimensional Photonic Crystal Microcavities for Chip-scale Laser Applications

Adam Mock¹ and Ling Lu²

¹Central Michigan University

²University of Southern California
USA

1. Introduction

1.1 Photonic crystals

In this chapter we will focus on two-dimensional photonic crystal devices and emphasize their use as building blocks in photonic integrated circuits with applications in high bandwidth optical communication systems. In particular we will discuss recent progress in designing high quality (Q) factor resonant cavities for building efficient micro- and nanocavity lasers. The first section will provide a brief overview of two-dimensional photonic crystals and motivate their use in photonic integrated circuits. This will be followed by a first principles derivation of the role of the Q factor in estimating laser threshold. We will then focus on the photonic crystal heterostructure cavity due to its exceptionally large Q factor. Its spectral and modal properties will be discussed, and its use as a high output power edge-emitting laser will be presented. We conclude with remarks on continuous wave laser operation via heat sinking lower substrates and the issue of out-of-plane loss.

The term photonic crystal refers to any structure with a periodic variation in its refractive index (John, 1987; Yablonovitch et al., 1991; Joannopoulos et al., 1995). The periodicity can be in one, two or three spatial dimensions and can introduce a photonic bandgap (a range of frequencies for which electromagnetic radiation is non-propagating) with the same dimensionality. The bandgap arises due to Bragg reflection and occurs when the spatial periodicity has a length scale approximately one half that of the incident electromagnetic radiation. This same phenomenon gives rise to the electronic bandgap in semiconducting materials. Examples of photonic crystal structures with periodicity in varying spatial dimensions are shown in Figure 1. One dimensional photonic crystals have found many technology applications in the form of Bragg reflectors which are part of the optical feedback mechanism in distributed feedback lasers (Kogelnik & Shank, 1971; Nakamura et al., 1973) and vertical cavity surface emitting lasers (Soda et al., 1979). Two and three dimensional photonic crystals have been the subject of intense research recently in areas related to sensing (Lončar et al., 2003; Chow et al., 2004; Smith et al., 2007), telecommunications (Noda et al., 2000; McNab et al., 2003; Bogaerts et al., 2004; Notomi et al., 2004; Noda et al., 2000; Jiang et al., 2005; Aoki et al., 2008), slow light (Vlasov et al., 2005; Krauss, 2007; Baba & Mori, 2007; Baba, 2008) and quantum optics (Yoshie et al., 2004; Lodahl et al., 2004; Englund et al., 2005).

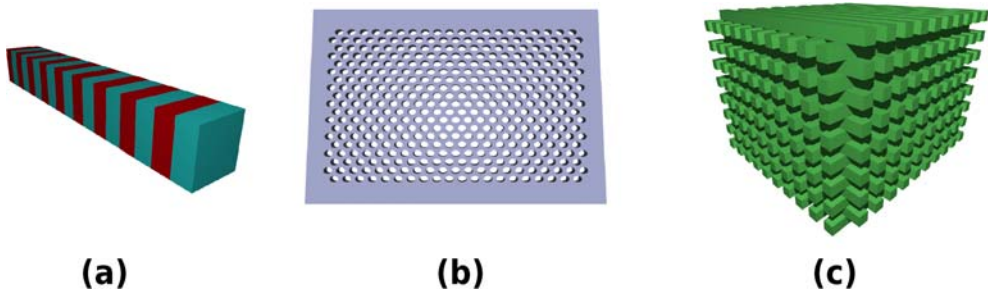


Fig. 1. Images depicting photonic crystals with periodicity in (a) one dimension, (b) two dimensions and (c) three dimensions.

Figure 1(b) displays a semiconductor slab perforated with a two-dimensional triangular array of air holes. Because of the periodic refractive index, the in-plane propagating modes of the slab can be characterized using Bloch's theorem. In the vertical, out-of-plane direction, the modes are confined via index guiding, and Figure 2(a) illustrates typical guided and radiation modes. These modes are peaked near the center of the slab and are either evanescent (guided) or propagating (radiation) out-of-plane. Figure 2(b) is a photonic band diagram corresponding to a photonic crystal structure similar to that shown in Figure 1(b) and Figure 2(a). The left vertical axis is written in terms of normalized frequency where a corresponds to the lattice constant of the photonic crystal, and c is the vacuum speed of light. The right vertical axis is denormalized and written in terms of free space wavelength using a lattice constant of $a = 400\text{nm}$. The photonic bandgap corresponds to the normalized frequency range 0.25-0.32 where there are no propagating modes in this structure. Using a lattice constant of $a = 400\text{nm}$ places the near infrared fiber optic communication wavelengths of $1.3\mu\text{m}$ (low-dispersion) and $1.5\mu\text{m}$ (low-loss) within the bandgap making this geometry amenable to applications in fiber optic communication systems. The shaded regions on the left and right sides of Figure 2(b) represent the projection of the light cone onto the various propagation directions which is a result of the vertical confinement mechanism being due to index guiding. Photonic crystal modes that overlap the shaded regions in Figure 2(b) correspond to the radiation modes in Figure 2(a). Figure 2(b) shows the dispersion for the three lowest frequency bands with transverse electric polarization (out-of-plane magnetic field has even vertical symmetry). Figure 2(c) illustrates a unit cell corresponding to a triangular lattice photonic crystal. The band diagram in Figure 2(b) was calculated using the three-dimensional finite-difference time-domain method (Taflove & Hagness, 2000). The computational domain is similar to that shown in Figure 2(c) where the in-plane boundaries are terminated using Bloch boundary conditions. More details about this approach can be found in (Kuang et al., 2007). Photonic crystal geometries represent complicated electromagnetic problems and almost always demand a numerical approach for their analysis. Several numerical methods for solving Maxwell's equations exist. Some examples include the finite-element method (Kim 2004), transmission line method (Benson et al., 2005), scattering based methods (Peterson et al., 1998; Sadiku 2000) and plane wave expansion methods for periodic structures (Joannopoulos et al., 1995; Sakoda 2001). In this work, we will be using the finite-difference time-domain method due to its generality, simplicity and linear scaling with problem size. For the band structure in Figure 2(b), the refractive index of the slab was set to $n = 3.4$, the hole radius to lattice constant ratio was set

to $r/a = 0.29$ and the slab thickness to lattice constant ratio was set to $d/a = 0.6$. These photonic crystal geometry parameters will hold for the rest of the devices analyzed in this chapter.

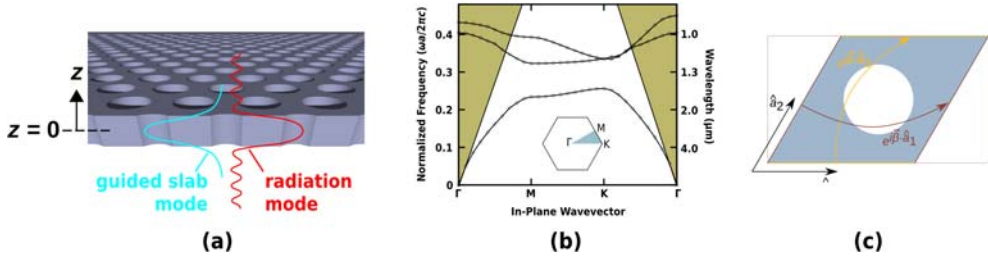


Fig. 2. (a) Cross section of a two-dimensional photonic crystal defined in a dielectric slab of finite thickness. The field distribution in the vertical direction for guided and radiation modes is shown. (b) Photonic band diagram for a two-dimensional photonic crystal defined in a single-mode slab. c denotes free space speed of light. a denotes the lattice constant. The diagram depicts the lowest three bands for the TE-like modes of the slab. The inset shows the region of the first Brillouin zone described by the dispersion diagram. (c) A unit cell of a triangular photonic crystal lattice and the phase relationships between the boundaries determined by Bloch's theorem.

1.2 Defects in two-dimensional photonic crystals

Much of the versatility and device applications of two-dimensional photonic crystal structures are associated with the introduction of defects into the periodic lattice. Figure 3(a) displays the out-of-plane component of the magnetic field of a typical mode associated with a photonic crystal waveguide formed by removing a single row of holes along the $\Gamma - K$ direction. For the TE-like modes of the slab, only the E_x , E_y and H_z fields are nonzero at the midplane, and H_z is displayed due to its scalar nature. It is clear that the mode is localized to the defect region along the y -direction due to the photonic crystal bandgap, and confinement along the z -direction is due to index guiding as discussed with regard to Figure 2(a). Figure 3(b) displays the unit cell used in the computation of the field shown in Figure 3(a). The finite-difference time-domain method was used with Bloch boundary conditions along the x -direction (Kuang et al., 2006). Figures 6(b) and 7 depict photonic crystal waveguide dispersion diagrams. The mode depicted in Figure 3(a) is associated with the lowest frequency band in the bandgap and a propagation constant of $\beta a = 1.9$. It has been shown that photonic crystal waveguides are capable of low loss optical guiding (McNab et al., 2003) and have the ability to redirect light along different directions in-plane with low loss waveguide bends (Shih et al., 2004).

Figure 3(c) displays the z -component of the magnetic field corresponding to a typical resonant mode of an L3 cavity (Akaahane et al., 2003, 2005). The L3 cavity is formed by removing three adjacent holes along the $\Gamma - K$ direction in a triangular photonic crystal lattice. The two dimensional in-plane confinement due to the photonic crystal bandgap is apparent. In the case of photonic crystal defect cavities, a single unit cell with Bloch boundary conditions is no longer applicable, and large three dimensional computational domains must be analyzed. Such a cavity can be used as an optical filter, an optical buffer or a laser.

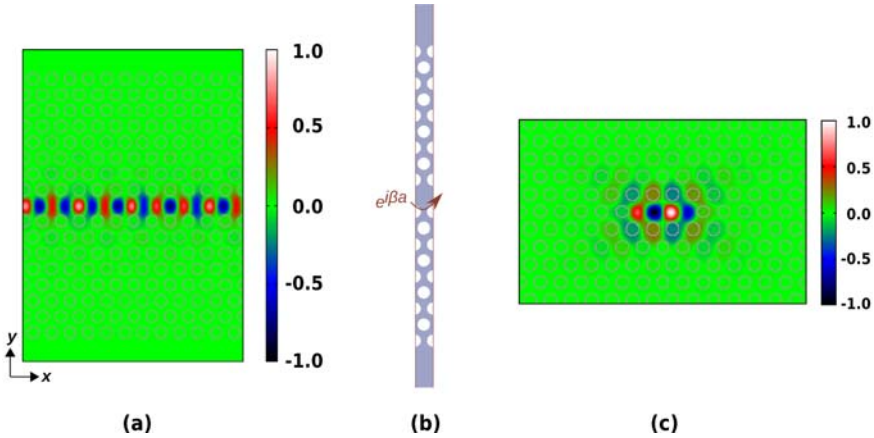


Fig. 3. (a) $H_z(x, y, z = 0)$ for a typical photonic crystal waveguide mode. $z = 0$ corresponds to the midplane of the slab as shown in Figure 2(a). (b) The unit cell of a photonic crystal waveguide and the phase relationship between the boundaries determined by Bloch's theorem. (c) $H_z(x, y, z = 0)$ for a typical L3 cavity mode.

1.3 Photonic integrated circuits

Photonic integration is analogous to the integration of electronic devices on a silicon chip. Typical microprocessors contain on the order of 10^9 transistors in an area on the order of 1cm^2 . Such dense device integration has resulted in microprocessors with exceptional functionality. And because the devices share a common substrate and metal wiring network, they can be mass produced with limited overhead costs.

Similar to electronic integrated circuits, photonic integrated circuits are useful for any application in which a large number of devices need to be contained in a confined space. Photonic integrated circuits have a variety of applications including telecommunications, sensing and imaging. In telecommunication systems photonic integrated circuits have the potential for lower cost systems due to reduced packaging costs, improved reliability due to reduced alignment errors and improved bandwidth through all optical signal processing. Another application of photonic integrated circuits is in optical buses in multicore computer architectures. The inter-core communication and off-chip memory access can be a performance bottleneck for applications with heavy memory access. Optics has the potential to improve memory access bandwidth due in part to its ability to transmit signals at multiple wavelengths through a single waveguide. It also has the advantage of operating at a lower temperature due to the absence of resistive heating.

Figure 4 shows a schematic diagram of a photonic crystal based photonic integrated circuit that includes sources, modulators, filters and detectors integrated on a single chip. This particular structure consists of a bus waveguide passing from left to right carrying modulated optical signals at wavelengths λ_1 and λ_2 . First, the signals encounter frequency selective filters which couple the filtered signal to an optical detector. On-chip lasers operating at λ_1 and λ_2 generate a new carrier beam which is modulated and rerouted to the bus waveguide. The input and output ports could lead to other on-chip processing or to coupled optical fibers. From this simple example, it is clear that photonic crystals offer a versatile platform for realizing a variety of different devices by local rearrangements of the

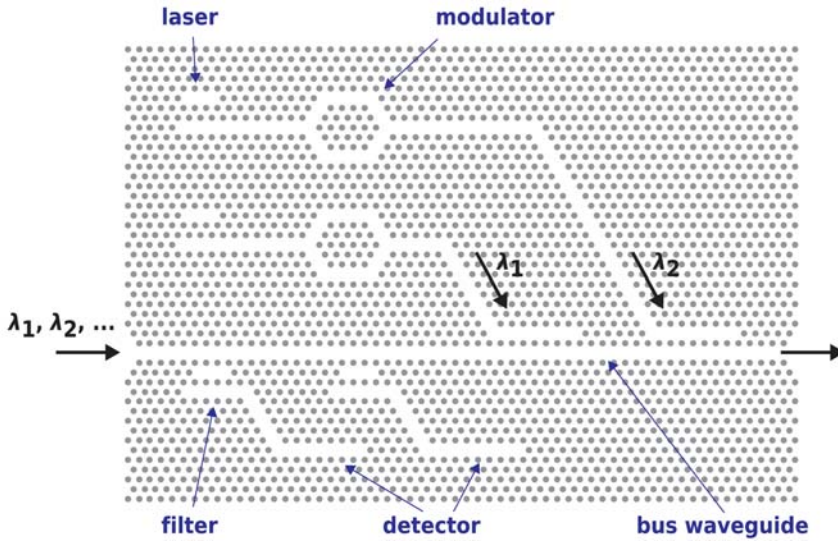


Fig. 4. Schematic diagram depicting a simple photonic crystal based photonic integrated circuit.

hole pattern. It is this flexibility along with their dispersive properties and high Q factor cavities that make photonic crystals an interesting candidate for photonic integration. Furthermore, devices based on photonic crystals have the potential to occupy smaller spaces than devices based on index guiding. In the remainder of this chapter we will focus our attention to aspects of designing photonic crystal cavities for on-chip laser sources.

2. High quality factor photonic crystal cavities

2.1 Role of the quality factor in determining laser threshold

The Q factor is a figure of merit used to quantify the radiation losses of an optical resonator. Formally it is defined by

$$Q = \omega_0 \frac{\langle U \rangle}{-\langle \frac{dU}{dt} \rangle} \quad (1)$$

where ω_0 is the resonance frequency, and the angled brackets denote a time-average over an integer number of optical periods. U represents the electromagnetic energy and is given by

$$U = \int \left[\frac{1}{2} \epsilon \vec{E} \cdot \vec{E} + \frac{1}{2} \mu \vec{H} \cdot \vec{H} \right] dV. \quad (2)$$

where ϵ represents the electric permittivity, \vec{E} represents the electric field, μ represents the magnetic permeability and \vec{H} represents the magnetic field. Equation 1 can be considered a first order ordinary differential equation in $\langle U \rangle$. Its solution is

$$\langle U(t) \rangle = \langle U(0) \rangle \exp(-\omega_0 t / Q). \quad (3)$$

Equation 3 tells us that the temporal decay of the electromagnetic energy stored in a large Q factor cavity will be slower than that of a low Q factor cavity. From Eq. 3 a photon lifetime can be defined as $\tau_p = Q/\omega_0$. This quantity is related to the average length of time that a photon spends inside a cavity. It is clear that a large Q factor results in a long photon lifetime.

In order to illustrate the precise role that the Q factor plays in designing efficient, low-threshold lasers, we will derive the laser threshold condition applicable to photonic crystal resonant cavities made from semiconductor active material (Mock & O'Brien, 2009a). Equation 4 is the Poynting theorem in its time averaged form and is a statement of electromagnetic energy conservation. \vec{S} is the Poynting vector and is given by $\vec{S} = \vec{E} \times \vec{H}$. Its closed surface integral represents the power radiated through the surface. P_a represents absorbed power which in the case of a semiconductor active material would occur in regions of the structure in which the carrier population is not inverted. P_s represents supplied power coming in the form of optical gain resulting from an external energy source.

$$\oint \langle \vec{S} \rangle \cdot d\vec{A} = -\left\langle \frac{\partial U}{\partial t} \right\rangle - \langle P_a \rangle + \langle P_s \rangle \quad (4)$$

If one considers a passive cavity in which $P_s = P_a = 0$ and substitutes dU/dt in Equation 1 into Equation 4 one gets

$$\oint \langle \vec{S}_m \rangle \cdot d\vec{A} = \omega_0 \frac{\langle U_m \rangle}{Q_p} \quad (5)$$

where the subscript m is used to specify that the Poynting vector and electromagnetic energy correspond to a specific mode m whose passive Q factor is given by Q_p . The basic idea behind laser threshold is that the optical loss mechanisms should be exactly compensated by an optical power source which comes in the form of optical gain (Schawlow & Townes, 1958). At threshold when the loss just equals the gain, the temporal rate of change of the energy in the cavity is zero, and we can set $dU/dt = 0$ in Equation 4. If we then use Equation 5 in Equation 4, the result is

$$\omega_0 \frac{\langle U_m \rangle}{Q_p} + \langle P_a \rangle = \langle P_s \rangle. \quad (6)$$

Equation 6 is the laser threshold condition. The first term on the left side represents passive cavity (radiative) losses. The second term represents active cavity (absorptive) losses. The right side represents the supplied power required to offset the optical losses. From the first term in Equation 6, it is apparent that the passive Q factor should be as large as possible so as to reduce the radiative losses and thus the power required to reach threshold. It should be noted, however, that a high Q factor cavity often results in reduced output power, and tradeoffs between low threshold and sufficient output power should be considered when designing a prospective cavity for chip-scale laser applications.

2.2 Two-dimensional photonic crystal cavities

Figure 5 displays four cavity designs as well as the evolution of their Q factors over the passed decade. Early photonic crystal cavities were formed by removing a single hole from

a uniform lattice (Painter et al., 1999; Ryu et al., 2002). More recently, linear defects have been shown to have higher Q factors than single missing hole cavities (Akahane et al., 2003, 2005), and the photonic crystal double heterostructure cavity has been shown to have the largest Q factor among two-dimensional photonic crystal cavities (Song et al., 2005; Tanaka et al., 2008). Because of its exceptionally high Q factor and small mode volume, the photonic crystal double heterostructure has been the subject of intense research for building efficient chip scale optical sources and will be highlighted in what follows.

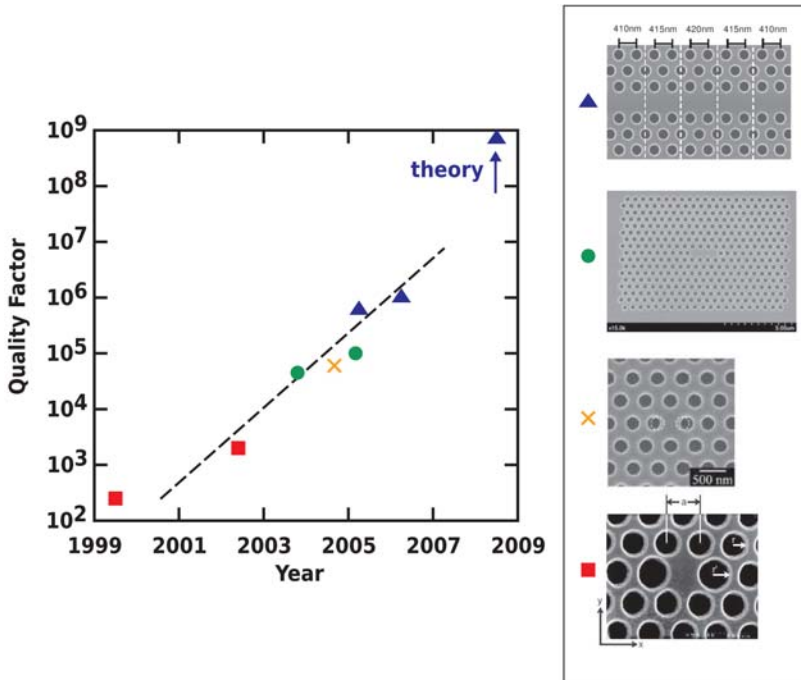


Fig. 5. Quality factor for different two-dimensional photonic crystal cavities as a function of time. Data points and figures come from (Painter et al., 1999; Ryu et al., 2002; Akahane et al., 2003; Zhang & Qiu, 2004; Nozaki & Baba, 2006; Akahane et al., 2005; Song et al., 2005; Asano et al., 2006; Tanaka et al., 2008)

3. Photonic crystal double heterostructure resonant cavities

3.1 Introduction

In 2005 Song et al. showed that a two-dimensional photonic crystal waveguide with a small, localized perturbation can form an ultra high Q factor cavity with a Q factor greater than 10^5 and a mode volume on the order of one cubic wavelength (Song et al., 2005, 2007). Such a cavity was termed a photonic crystal double heterostructure and is depicted in Figure 6. The cavity is formed from an otherwise uniform photonic crystal waveguide by enlarging the lattice constant along the x -direction of the light colored air holes. Below the schematic diagram, the resulting photonic band structure is shown illustrating the formation of a photonic well along the x -direction. Further experimental work on these cavities has

demonstrated devices with passive Q factors as large as 10^6 (Asano et al., 2006). Since these initial reports, several groups have reported forming high Q factor photonic crystal double heterostructure cavities through a variety of methods including local modulation of a photonic crystal line defect width (Kuramochi et al., 2006), local air-hole infiltration (Smith et al., 2007), photosensitive materials (Tomljenovic-Hanic et al., 2007), effective index change through micro-fiber coupling (Kim et al., 2007) and local modulation of the hole radii (Kwon et al., 2008b). A numerical analysis showed that Q factors as high as 10^9 are possible with a tapered perturbation (Tanaka et al., 2008). The ultra high Q factors and cubic wavelength mode volumes along with the waveguide-like shape of the cavities have made them attractive for a variety of applications including chemical sensing (Kwon et al., 2008a), slow light (Tanabe et al., 2007; Takahashi et al., 2007), elements of coupled resonator optical waveguides (O'Brien et al., 2007) and edge-emitting lasers (Shih, Kuang, Mock, Bagheri, Hwang, O'Brien & Dapkus, 2006; Shih, Mock, Hwang, Kuang, O'Brien & Dapkus, 2006; Yang et al., 2007; Lu et al., 2007, 2008; Lu, Mock, Shih, Hwang, Bagheri, Stapleton, Farrell, O'Brien & Dapkus, 2009).

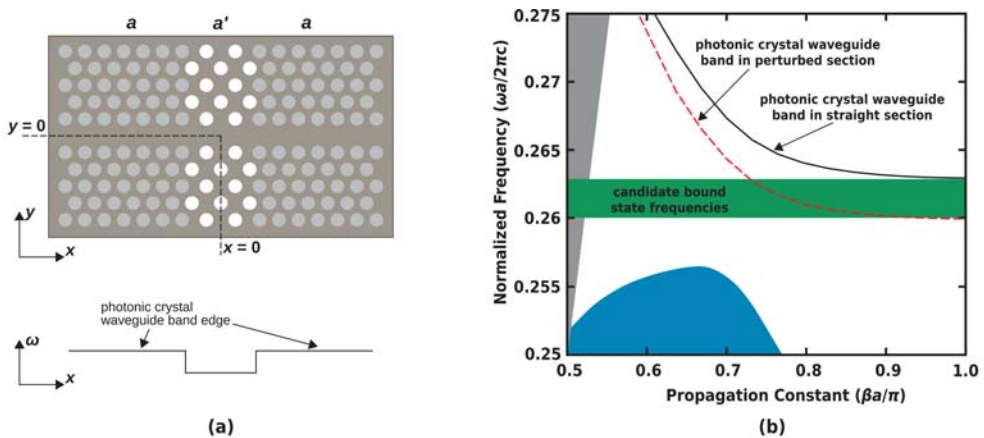


Fig. 6. (a) Schematic diagram of a photonic crystal double heterostructure resonant cavity formed in a uniform single line defect waveguide by increasing the lattice constant of the light colored holes along the x -direction. The resulting photonic well diagram is illustrated below. (b) Photonic crystal waveguide dispersion diagram depicting the photonic crystal waveguide bands associated with the straight (black, solid) and perturbed (red, dashed) portions of the waveguide. The waveguide frequencies of the perturbed section that fall into the mode gap of the straight waveguide are labeled "candidate bound state frequencies." The blue region denotes the photonic crystal cladding modes, and the gray region denotes the light cone.

3.2 Spectral and modal properties

When the lattice constant is locally increased, it shifts the frequencies of the waveguide band associated with the perturbed region to lower frequencies as shown in Figure 6(b). The bound state will oscillate near frequencies of the perturbed waveguide section that fall into the mode gap of the uniform waveguide sections. Candidate frequencies for bound state resonances are labeled in Figure 6(b). Only below the minima of the dispersion relation in

the uniform photonic crystal waveguide regions is there a possibility for a mode to exist in the central region without the possibility of there simultaneously being a mode in the cladding at the same frequency a small distance in wavevector away. In other words, only in these cases is there no mode that is nearby (in the wavevector sense) in the cladding at the same frequency (Mock et al., 2006, 2008). This mode formation is analogous to the formation of bound states in electronic heterostructures at the extrema of the electronic dispersion relations.

Figure 7 is a comparison between the spectral features of a photonic crystal double heterostructure resonance spectrum and the frequency axis of the photonic crystal waveguide dispersion diagram corresponding to the underlying straight waveguide. The red dotted lines illustrate that the bound state resonance frequencies occur just below the waveguide dispersion minima. The resonance spectrum was obtained by taking a discrete Fourier transformation of a 2×10^5 element time sequence. The time sequence was calculated via the three dimensional finite-difference time-domain method. The computational domain included 20 uniform photonic crystal cladding periods on either side of the central defect region along the x -direction and 8 photonic crystal layers above and below the central waveguide core along the y -direction. This geometry was discretized with $950 \times 340 \times 200$ discretization points along the $x \times y \times z$ directions and parallelized using $11 \times 4 \times 3$ processors (132 total processors) along the $x \times y \times z$ directions. The geometry was discretized using 20 points per lattice constant (a). The lattice constant of the perturbed region was increased by 5% along the x -direction.

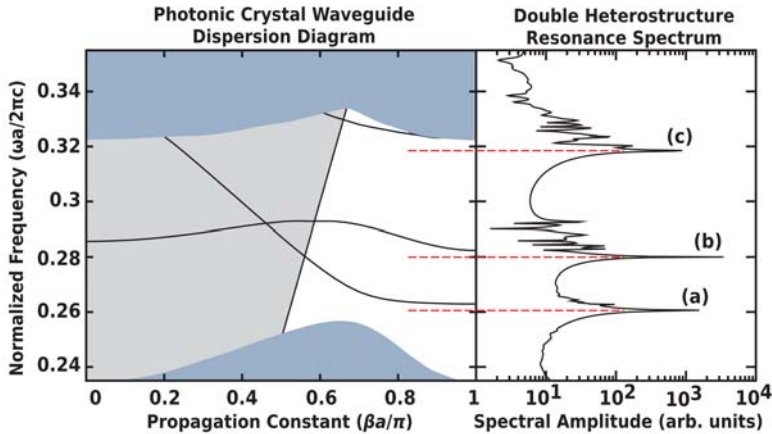


Fig. 7. Left: photonic crystal waveguide dispersion diagram. Black lines correspond to the photonic crystal waveguide dispersion bands. Blue regions denote photonic crystal cladding modes. The gray region denotes the light cone projection. Right: photonic crystal double heterostructure resonant spectrum. Dashed lines illustrate correspondence between heterostructure bound state frequencies and waveguide dispersion extrema.

Figure 8 depicts the z -component of the magnetic field for the bound state resonances labeled in Figure 7. These mode profiles may be interpreted as consisting of the waveguide mode of the underlying straight waveguide multiplied by a confining envelope function centered at the perturbation. It is interesting to point out that mode (c) exhibits significant

extension into the photonic crystal cladding. This can be attributed to the close proximity of the corresponding photonic crystal waveguide band to the photonic crystal cladding modes in Figure 7. To the right of each $H_z(x, y, z = 0)$ mode profile is the corresponding spatial Fourier transform. Specifically, $\log(|FT(E_x)|^2 + |FT(E_y)|^2)$ is plotted where FT stands for Fourier transform. The two-dimensional spatial Fourier transform yields the spatial wavevector components that make up the bound state resonance. The spatial wavevector distributions are centered at $\beta_x = \pm\pi/a$. This is consistent with the observation that bound state resonance frequencies occur near the waveguide dispersion minima which coincide with the Brillouin zone boundary at $\beta_x = \pm\pi/a$ for this particular waveguide.

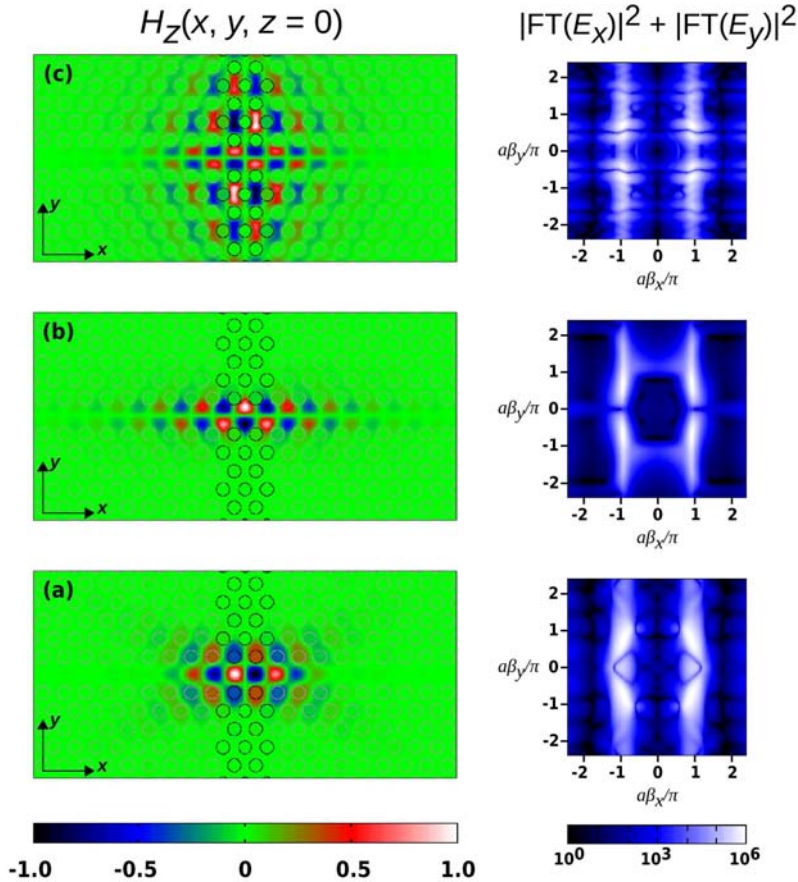


Fig. 8. Left: $H_z(x, y, z = 0)$ for the three modes summarized in Table 1. Right: spatial Fourier transform $\log(|FT(E_x)|^2 + |FT(E_y)|^2)$ of each mode illustrating the distribution of spatial wavevectors making up the different resonant modes.

Table 1 summarizes the normalized resonance frequencies of the three modes shown in Figure 8. The resonance frequencies and Q factors were obtained using the Padé interpolation method (Mock & O'Brien, 2008). It is clear that the bound state resonance

frequencies fall just below the photonic crystal waveguide band edge. Mode (a) has the largest Q factor and will be featured in the remainder of this chapter.

Mode	Resonance Frequency	Bandedge Frequency	Q factor
(a)	0.2606	0.2629	336,700
(b)	0.2800	0.2824	10,800
(c)	0.3184	0.3227	8,250

Table 1. Summary of Q factors and resonant frequencies for the resonant modes associated with a photonic crystal heterostructure cavity.

3.3 Higher-order bound states

The previous section discussed a photonic crystal double heterostructure cavity resulting from a 5% lattice constant stretching along the x -direction. Figure 9 shows several interesting features of the high Q factor mode in Table 1 as the degree of perturbation is varied. First, the Q factor exhibits a strong dependence on the percent lattice constant increase. For very shallow perturbations (<3%), Q factors in excess of one million are predicted. Whereas for perturbations exceeding 20%, the Q factor dips below one thousand. Intuitively, one would expect that by increasing the lattice constant perturbation, the photonic well is deepened which would lead to improved confinement. It turns out that deepening the well makes the transition between the straight waveguide and the perturbation region more abrupt and introduces high spatial frequencies into the envelope function of the mode along the x -direction (Akhahane et al., 2003). Because these modes have Fourier space distributions centered near $\beta_x = \pi/a$, large spatial frequencies in the envelope function get shifted to regions in Fourier space near $\beta_x = 0$. Fourier components inside the light cone centered at the origin in Fourier space radiate out-of-plane, and this loss mechanism dominates the overall loss properties of the mode. Researchers have investigated designs that smoothen the transition between the straight waveguide regions and the perturbation region and have obtained improved Q factors as a result (Akhahane et al., 2005; Song et al., 2005).

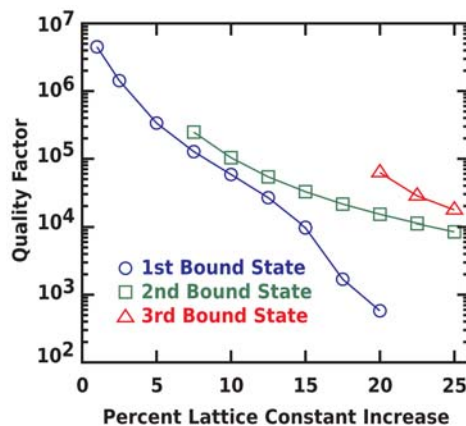


Fig. 9. Q factor versus perturbation depth for the first, second and third order bound states.

The second interesting feature of Figure 9 is the presence of higher order bound states. For perturbations greater than 7.5%, the cavity supports both a first order and a second order bound state. For perturbations greater than 20%, the cavity supports three bound states. The Q factors of the higher order bound state resonances exhibit a similar dependence on percent lattice constant increase as the first order bound state. It should also be pointed out that for a given perturbation, the highest order bound state has the largest Q factor. Figure 10 displays the z -component of the magnetic field of the first three bound states associated with a heterostructure cavity. Also shown are the envelope functions obtained by extracting

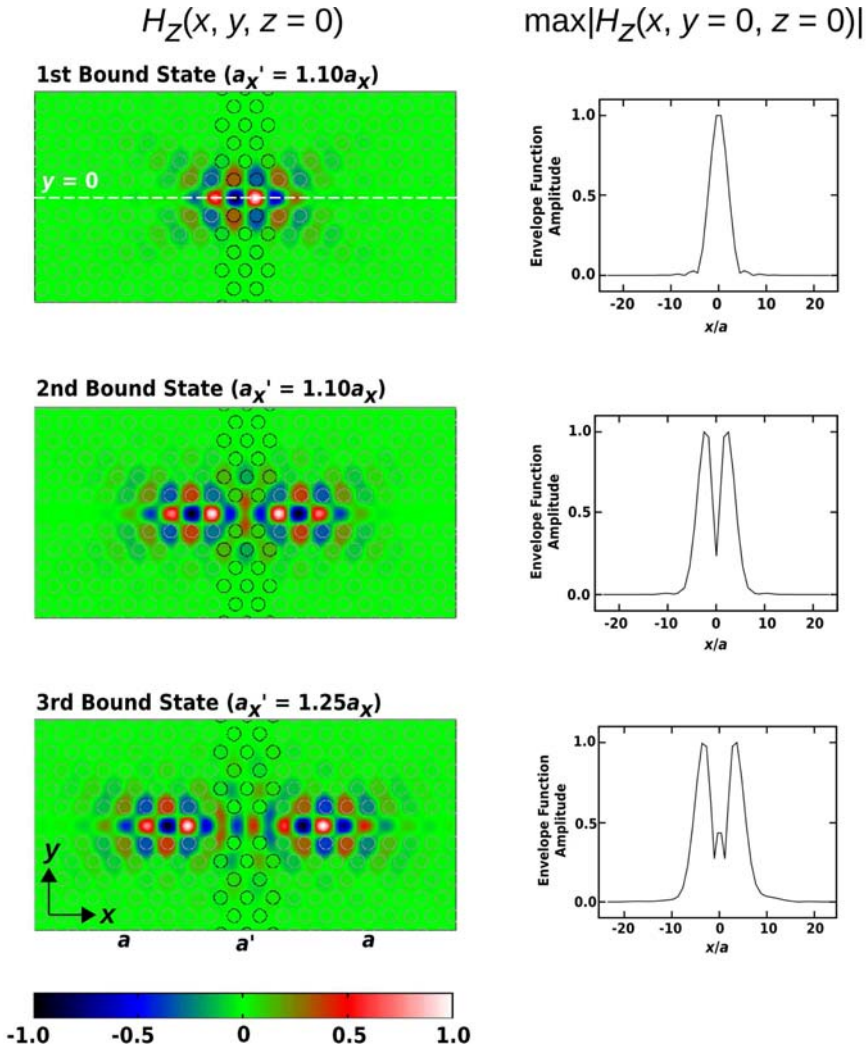


Fig. 10. Left: $H_z(x, y, z = 0)$ field distributions for the first, second and third order bound states. Right: field envelopes extracted from $|H_z(x, y = 0, z = 0)|$.

the maxima of $|H_z(x, y = 0, z = 0)|$ (the dotted white line in the top image of Figure 10 depicts the contour along which the maxima were measured). The envelope functions show a similar behavior to the wavefunction solutions corresponding to a quantum well problem in quantum mechanics.

From a technology perspective, if one chooses to work with a cavity that supports multiple bound states, then it is useful to be able to enhance one mode relative to the others. From Equation 6, one sees that the mode with the largest Q factor will be the first to reach threshold if the cavity is multimoded. However, from Figure 10, the various bound states have different spatial mode distributions and thus different overlap integrals with the spatial gain distribution. For instance, an optical pump beam directly centered on the heterostructure cavity will preferentially pump the first order bound state, and this mode could reach threshold first even though it has a smaller Q factor than the second order bound state. In order to get around this issue one can introduce cavity modifications that significantly reduce the Q factors of the unwanted modes while leaving the Q factor of the featured mode intact. Such a mode discrimination scheme improves side mode suppression as well.

One strategy to perform mode discrimination is to place extra holes in the cavity near the maxima of the electric field corresponding to the mode we wish to suppress. This enhances out-of-plane radiation and lowers the Q factor (Kuang et al., 2005). Figure 11 displays modified cavities that were fabricated in a 240-nm-thick suspended InGaAsP membrane containing four compressively strained quantum wells. The semiconductor dry-etch was done in an inductively coupled plasma etcher using BCl_3 chemistry at 165°C . The rest of the fabrication processes are the same as those in (Shih, Kuang, Mock, Bagheri, Hwang, O'Brien & Dapkus, 2006). The inset of Figure 11(a) displays a scanning electron micrograph of a cavity with a 10% perturbation which supports both the first order and the second order bound states. The inset of Figure 11(b) illustrates a cavity with holes placed at $x = \pm 2.4a$ to suppress the second order bound state, and Figure 11(c) illustrates a cavity with a hole placed at $x = 0$ to suppress the first order bound state (Mock et al., 2009).

The devices were optically pumped at room temperature by an 850 nm diode laser at normal incidence with an 8 ns pulse width and 1% duty cycle. The size of the pump spot was about $2 \mu\text{m}$ in diameter. The lower spectrum in Figure 11(a) is the single-mode lasing spectrum operating in the first bound state, while the upper multimode lasing spectrum shows the existence of the second bound state approximately 20 nm away from the first one when the pump spot is slightly moved off the device center along the waveguide core. The two modified structures in Figure 11(b) and (c) both operate in stable single-mode operation with respect to pump beam location. Their lasing wavelengths line up with the first and second bound states lasing in the unmodified structure. All four lasing spectra were taken at the peak incident power of 1.7mW. The broad resonance peak between 1.40 and $1.45 \mu\text{m}$ corresponds to a higher order waveguide dispersion band. Figure 11(d) depicts the light-in-light-out (L-L) curves of the three lasers shown in (a)-(c). They have almost identical thresholds but different slopes, indicating the same amount of total optical loss but different portions of collected laser power. It is possible that the extra holes are causing some excess vertical scattering that is collected by the collection setup.

3.4 Edge-emitting lasers

As mentioned earlier in this chapter, large Q factor cavities lead to reduced laser thresholds resulting from reduced radiative losses. However, reduced radiative losses also reduce the

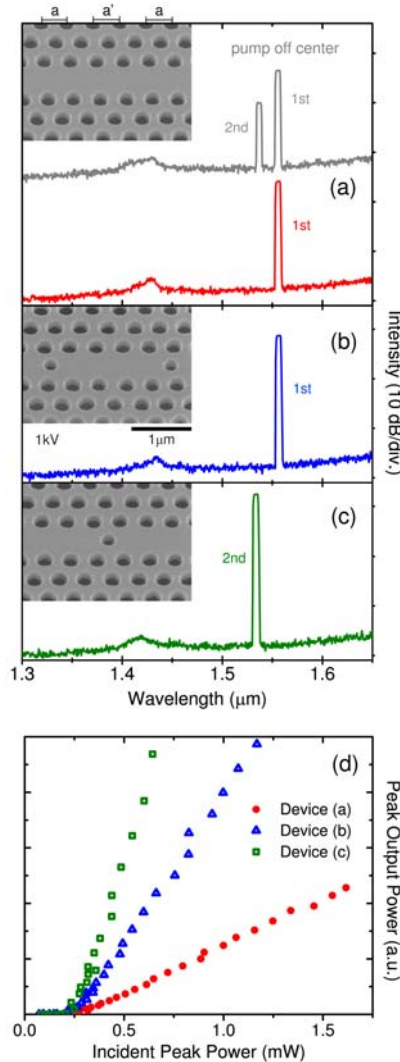


Fig. 11. (a)-(c) Lasing spectra of three double-heterostructure lasers with 10% perturbation ($a_x' = 1.10a_x$). Their SEM images are shown as insets. (d) Light-in-light-out curves of the lasers in (a)-(c).

output power of a laser for a given pump level. For applications related to integrated photonics, it is important to have sufficient output power for efficient on-chip detection with a large signal-to-noise ratio and low bit error rate. Fortunately, high Q factor cavities give the designer freedom to lower the Q factor intentionally by introducing losses in a preferential radiation direction. For photonic integrated circuits, the preferential output direction is in-plane. Because the photonic crystal double heterostructure cavity is formed from a perturbation of a straight waveguide, the in-plane losses can be enhanced along the

waveguide direction by reducing the number of uniform waveguide periods cladding the perturbation region. Figure 12 displays a finite-difference time-domain simulation of a fabricated heterostructure cavity in which several uniform photonic crystal waveguide cladding periods on one side of the structure have been removed. The geometry was defined in the numerical simulation from a scanning electron micrograph of a fabricated device. For this structure, only five uniform waveguide periods remain between the etched facet and the perturbation region. In excess of 100 microWatts of peak power was measured from this cavity (Lu, Mock, Shih, Hwang, Bagheri, Stapleton, Farrell, O'Brien & Dapkus, 2009). One issue with this structure is that the output power is diffracting at relatively large angles, so that our measurement setup did not collect all of the edge-emitted output power. More recent cavity designs have improved the directionality and have demonstrated output powers in excess of 500 microWatts (Lu, Mock, Hwang, O'Brien & Dapkus, 2009). It should be noted that in a real integrated photonics application, these cavities would be coupled to in-plane waveguides. Coupling efficiencies between defect cavities and photonic crystal waveguides as high as 90% have been reported (Nozaki & Watanabe, 2008) which suggests that over a milliWatt of power could be coupled to an in-plane waveguide. These results strengthen the technological viability of photonic crystal lasers as commercial on-chip sources.

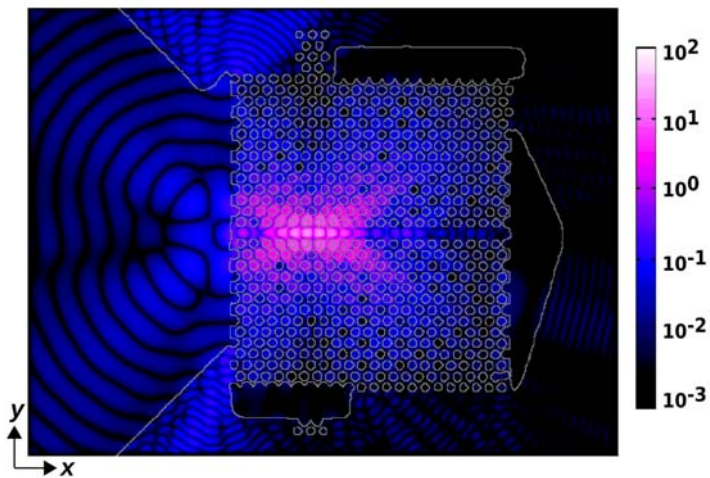


Fig. 12. Finite-difference time-domain calculation of the lasing mode in a fabricated edge-emitting heterostructure laser. $|H_z(x, y, z = 0)|$ is plotted.

4. Heat sinking dielectric substrates

In addition to demonstrating that photonic crystal lasers are capable of outputting sufficient output power, showing that these lasers are capable of continuous wave (CW) operation at room temperature and above is another important step in advancing the commercial viability of these sources. The experimental lasing results described thus far correspond to a pulsed optical pump. As mentioned previously, these cavities are formed in thin, suspended membranes which makes it difficult for the material to dissipate heat buildup in the vertical direction. Furthermore, the lattice of airholes reduces the effective thermal conductivity in-

plane further reducing the ability of these lasers to dissipate heat. Pulsed pumping allows sufficient carrier excitation for the laser to reach threshold, but the pump beam is on for short enough time periods that the gain properties of the active material are not degraded due to heating.

One approach to achieving CW operation is to grow or bond the semiconductor active material to a thermally conductive lower substrate to aid in heat dissipation (Cao et al., 2005). Two candidate materials include silicon dioxide whose thermal conductivity is 0.014W/cm-K and sapphire whose thermal conductivity is 0.34W/cm-K . These thermal conductivities are significantly larger than that of air alone (0.00024W/cm-K). The trade-off associated with introducing a thermally conductive lower substrate is that the index contrast between the semiconductor slab and the vertical cladding structure is reduced which increases the optical leakage into the substrate. Figure 13 depicts the total Q factor of the heterostructure cavity as a function of the index of the lower substrate. Also depicted are the directional Q factors characterizing radiative losses into the waveguide direction (WG), photonic crystal cladding (PC), air and substrate. Because the directional Q factors add as inverses to express the total Q factor, the lowest directional Q factor will represent the dominant loss mechanism. In this case, it is confirmed that radiation into the substrate is the dominant loss mechanism as the substrate index is increased. The refractive indices of silicon dioxide and sapphire are 1.45 and 1.74, respectively. From Figure 13, the total Q factor has dropped to 4600 for $n=1.45$ and 610 for $n=1.74$. Previous studies have found that the minimum Q factor required for CW lasing in sapphire bonded cavities is 1000 (Shih et al., 2006). One sees that the photonic crystal heterostructure cavity is predicted to have a Q factor below 1000 when its substrate refractive index is consistent with that of sapphire suggesting that this configuration is not capable of achieving CW threshold when bonded to sapphire.

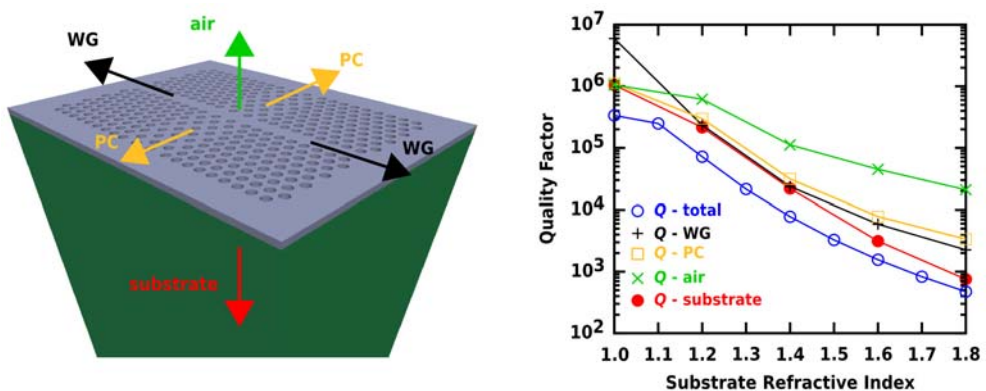


Fig. 13. (a) Depiction of a photonic crystal heterostructure cavity bonded or grown on a lower substrate. Radiation directions are indicated. (b) Q factor versus substrate refractive index for the total Q factor as well as the directional Q factors.

In order to reduce optical radiation into the substrate, an alternative cavity design based on introducing a glide-plane along the waveguide direction has been proposed (Kuang & O'Brien, 2004; Mock & O'Brien, 2009b). Intuitively, the glide-plane introduces a phase shift between the fields on either side of the waveguide core, so that when the two fields combine

on-axis, they interfere destructively, and the out-of-plane radiation is reduced. This configuration is known as a type B photonic crystal heterostructure. A schematic of the cavity is shown in Figure 14(a) along with a directional loss analysis in Figure 14(b). It should be noted that the cavity analysed in Figure 14(b) included a tapered perturbation in which intermediate stretchings of 2.5% were included on either side of the 5% perturbation. The motivation for this was to reduce the glide-plane symmetry breaking which reduced in-plane losses. It is apparent from the directional loss analysis that for substrate refractive indices between 1.0 and 1.5, the dominant loss mechanism is in-plane along the waveguide direction. The total Q factor remains flat over this range of substrate refractive indices due to the improved susceptibility to out-of-plane radiation. For substrate refractive indices greater than 1.5, the substrate losses dominate. It should be pointed out that the type B heterostructure has a total Q factor in excess of 1000 when its substrate refractive index is consistent with that of sapphire making this geometry a promising candidate for edge-emitting photonic crystal lasers operated under CW conditions.

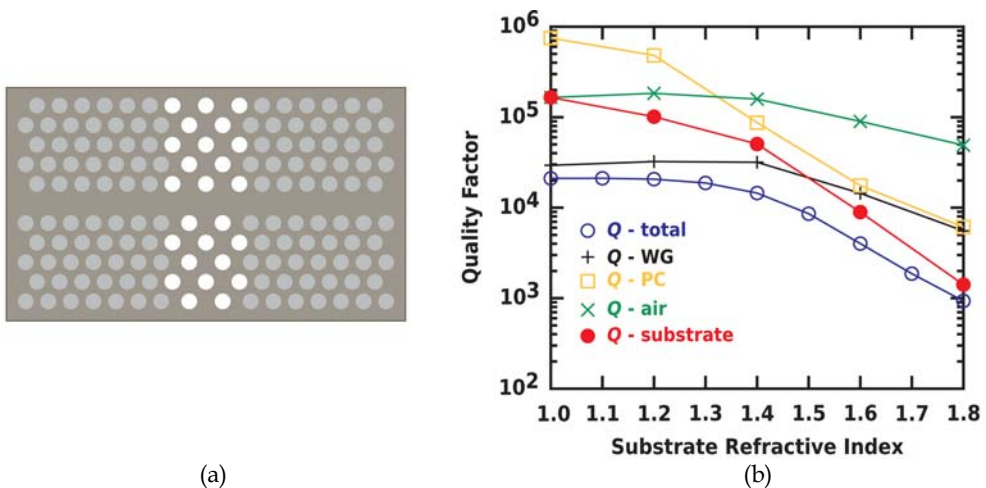


Fig. 14. (a) Schematic diagram of a type B heterostructure cavity. (b) Q factor versus substrate refractive index for the total Q factor as well as the directional Q factors. Radiation directions are the same as those in Figure 13(a).

5. Conclusion

In this chapter we have highlighted recent progress in the design of high Q factor two dimensional photonic crystal cavities for on-chip lasing. The photonic crystal double heterostructure was featured due to its ultra high Q factor and small mode volume. A first principles derivation of the laser threshold condition was presented which motivated using a large Q factor cavity to achieve low threshold. This was contrasted with the issue of output power in which the cavity Q factor was intentionally lowered in order to extract higher output power. The ability to discriminate between modes when these cavities supported multiple bound states was demonstrated. Finally issues of heat sinking were discussed, and the out-of-plane loss properties associated with dielectric lower substrates were quantified.

A novel cavity based on introducing a glide-plane symmetry was shown to have reduced out-of-plane losses.

6. References

- Akahane, Y., Asano, T., Song, B.-S. & Noda, S. (2003). High- Q photonic nanocavity in a two-dimensional photonic crystal, *Nature* 425: 944–947.
- Akahane, Y., Asano, T., Song, B.-S. & Noda, S. (2005). Fine-tuned high- Q photonic-crystal nanocavity, *Optics Express* 13(4): 1202–1214.
- Aoki, K., Guimard, D., Nishioka, M., Nomura, M., Iwamoto, S. & Arakawa, Y. (2008). Coupling of quantum dot light emission with three-dimensional photonic crystal nanocavity, *Nature Photonics* 2: 688–692.
- Asano, T., Song, B.-S. & Noda, S. (2006). Analysis of the experimental Q factors (~ 1 million) of photonic crystal nanocavities, *Optics Express* 14(5): 1996–2006.
- Baba, T. (2008). Slow light in photonic crystals, *Nature Photonics* 2: 465–473.
- Baba, T. & Mori, D. (2007). Slow light engineering in photonic crystals, *Journal of Physics D* 40: 2659–2665.
- Benson, T.M., Sewell, P., Boriskina, S. V., Janyani, V., Al-Jarro, A., Vukovic, A., Sakhnenko, N., Smotrova, E. I., Nosich, A. I. & Nerukh, A. G. (2005). Microcavities: An inspiration for advanced modelling techniques, *7th International Conference on Transparent Optical Networks*, Barcelona, Spain, pp. 272–275.
- Bogaerts, W., Taillaert, D., Luyssaert, B., Dumon, P., Van Campenhout, J., Bienstman, P., Van Thourhout, D. & Baets, R. (2004). Basic structures for photonic integrated circuits in silicon-on-insulator, *Optics Express* 12(8): 1583–1591.
- Cao, J. R., Kuang, W., Wei, Z.-J., Choi, S.-J., Yu, H., Bagheri, M., O'Brien, J. D. & Dapkus, P. D. (2005). Sapphire-bonded photonic crystal microcavity lasers and their far-field radiation patterns, *Photonics Technology Letters* 17(1): 4–6.
- Chow, E., Grot, A., Mirkarimi, L. W., Sigalas, M. & Girolami, G. (2004). Ultracompact biochemical sensor built with two-dimensional photonic crystal microcavity, *Optics Letters* 29(10): 1093–1095.
- Englund, D., Fattal, D., Waks, E., Solomon, G., Zhang, B., Nakaoka, T., Arakawa, Y., Yamamoto, Y. & Vučković, J. (2005). Controlling the spontaneous emission rate of single quantum dots in a two-dimensional photonic crystal, *Physical Review Letters* 95: 013904 1–4.
- Jiang, Y., Jiang, W., Gu, L., Chen, X. & Chen, R. T. (2005). 80-micron interaction length silicon photonic crystal waveguide modulator, *Applied Physics Letters* 87: 221105.
- Joannopoulos, J. D., Meade, R. D. & Winn, J. N. (1995). *Photonic Crystals*, Princeton University Press, Princeton, NJ.
- John, S. (1987). Strong localization of photons in certain disordered dielectric superlattices, *Physical Review Letters* 58(23): 2486–2489.
- Kim, M.-K., Hwang, I.-K., Seo, M.-K. & Lee, Y.-H. (2007). Reconfigurable microfiber-coupled photonic crystal resonator, *Optics Express* 15(25): 17241–17247.
- Kim, W. J. (2004). *Ph. D Thesis*, University of Southern California, Los Angeles, CA.
- Kogelnik, H. & Shank, C. V. (1971). Stimulated emission in a periodic structure, *Applied Physics Letters* 18(4): 152–154.

- Krauss, T. F. (2007). Slow light in photonic crystal waveguides, *Journal of Physics D* 40: 2666–2670.
- Kuang, W., Cao, J. R., Choi, S.-J., O'Brien, J. D. & Dapkus, P. D. (2005). Modified suspended membrane photonic crystal d3 laser cavity with improved sidemode suppression ratio, *Optics Express* 17(5): 941–943.
- Kuang, W., Kim, W. J., Mock, A. & O'Brien, J. D. (2006). Propagation loss of line-defect photonic crystal slab waveguides, *IEEE Journal of Selected Topics in Quantum Electronics* 12(6): 1183–1195.
- Kuang, W., Kim, W. J. & O'Brien, J. D. (2007). Finite-difference time domain method for nonorthogonal unit-cell two-dimensional photonic crystals, *Journal of Lightwave Technology* 25(9): 2612–2617.
- Kuang, W. & O'Brien, J. (2004). Reducing the out-of-plane radiation loss of photonic crystal waveguides on high-index substrates, *Optics Letters* 29(8): 860–862.
- Kuramochi, E., Notomi, M., Mitsugi, S., Shinya, A. & Tanabe, T. (2006). Ultrahigh-Q photonic crystal nanocavities realized by the local width modulation of a line defect, *Applied Physics Letters* 88: 041112-1–041112-3.
- Kwon, S.-H., Sünnner, T., Kamp, M. & Forchel, A. (2008a). Optimization of photonic crystal cavity for chemical sensing, *Optics Express* 16(16): 11709–11717.
- Kwon, S.-H., Sünnner, T., Kamp, M. & Forchel, A. (2008b). Ultrahigh-Q photonic crystal cavity created by modulating air hole radius of a waveguide, *Optics Express* 16(7): 4605–4614.
- Lodahl, P., van Driel, A. F., Nikolaev, I. S., Irman, A., Overgaag, K., Vanmaekelbergh, D. & Vos, W. L. (2004). Controlling the dynamics of spontaneous emission from quantum dots by photonic crystals, *Nature* 430: 654–657.
- Lončar, M., Scherer, A. & Qiu, Y. (2003). Photonic crystal laser sources for chemical detection, *Applied Physics Letters* 82(26): 4648–4650.
- Lu, L., Mock, A., Bagheri, M., Hwang, E. H., O'Brien, J. D. & Dapkus, P. D. (2008). Double heterostructure photonic crystal lasers with reduced threshold pump power and increased slope efficiency obtained by quantum well intermixing, *Optics Express* 16(22): 17342–17347.
- Lu, L., Mock, A., Hwang, E. H., O'Brien, J. D. & Dapkus, P. D. (2009). High peak power efficient edge-emitting photonic crystal nanocavity lasers, *Integrated Photonics and Nanophotonics Research and Applications Topical Meeting*, Optical Society of America, Honolulu, Hawaii, USA, p. ITuB3.
- Lu, L., Mock, A., Yang, T., Shih, M. H., Hwang, E. H., Bagheri, M., Stapleton, A., Farrell, S., O'Brien, J. D. & Dapkus, P. D. (2009). 120 μW peak output power from edge-emitting photonic crystal double heterostructure nanocavity lasers, *Applied Physics Letters* 94(13): 111101.
- Lu, L., Yang, T., Mock, A., Shih, M. H., Hwang, E. H., Bagheri, M., Stapleton, A., Farrell, S., O'Brien, J. D. & Dapkus, P. D. (2007). 100 μW edge-emitting peak power from a photonic crystal double-heterostructure laser, *Conference on Lasers and Electro-Optics Technical Digest*, Baltimore, MD, p. CMV3.
- McNab, S. J., Moll, N. & Vlasov, Y. A. (2003). Ultra-low loss photonic integrated circuit with membrane-type photonic crystal waveguides, *Optics Express* 11(22): 2927–2939.

- Mock, A., Kuang, W., Shih, M. H., Hwang, E. H., O'Brien, J. D. & Dapkus, P. D. (2006). Spectral properties of photonic crystal double-heterostructure resonant cavities, *Laser and Electro-Optics Society Annual Meeting Technical Digest*, Montreal, Canada, p. ML4.
- Mock, A., Lu, L., Hwang, E. H., O'Brien, J. & Dapkus, P. D. (2009). Modal analysis of photonic crystal double-heterostructure laser cavities, *Journal of Selected Topics in Quantum Electronics* 15(3): 892–900.
- Mock, A., Lu, L. & O'Brien, J. D. (2008). Spectral properties of photonic crystal double heterostructure resonant cavities, *Optics Express* 16(13): 9391–9397.
- Mock, A. & O'Brien, J. D. (2008). Convergence analysis of padé interpolation for extracting large quality factors in photonic crystal double heterostructure resonant cavities, *Conference on Numerical Simulation of Optoelectronic Devices Technical Digest*, Nottingham, England, p. TuB3.
- Mock, A. & O'Brien, J. D. (2009a). Photonic crystal laser threshold analysis using 3-d fdtd with a material gainmodel, *Integrated Photonics and Nanophotonics Research and Applications Topical Meeting*, Optical Society of America, Honolulu, Hawaii, USA, p. ITuD6.
- Mock, A. & O'Brien, J. D. (2009b). Quality factor dependence on vertical slab structure in photonic crystal double heterostructure resonant cavities, *Integrated Photonics and Nanophotonics Research and Applications Technical Digest*, Honolulu, HI, p. IMF2.
- Nakamura, M., Yariv, A., Yen, H. W., Somekh, S. & Garvin, H. L. (1973). Optically pumped gaas surface laser with corrugation feedback, *Applied Physics Letters* 22(10): 515–516.
- Noda, S., Tomoda, K., Yamamoto, N. & Chutinan, A. (2000). Full three-dimensional photonic bandgap crystals at near-infrared wavelengths, *Science* 289(5479): 604–606.
- Notomi, M., Shinya, A., Mitsugi, S., Kuramochi, E. & Ryu, H.-Y. (2004). Waveguides, resonators and their coupled elements in photonic crystal slabs, *Optics Express* 12(8): 1551–1561.
- Nozaki, K. & Baba, T. (2006). Laser characteristics with ultimate-small modal volume in photonic crystal slab point-shift nanolasers, *Applied Physics Letters* 88: 211101–1–211101–3.
- Nozaki, K. & Watanabe, HidekiBaba, T. (2008). Hundred micro-watts peak output power from an edge-emitting photonic crystal double-heterostructure laser, *Applied Physics Letters* 92(2): 021108.
- O'Brien, D., Settle, M. D., Karle, T., Michaeli, A., Salib, M. & Krauss, T. F. (2007). Coupled photonic crystal heterostructure nanocavities, *Optics Express* 15(3): 1228–1233.
- Painter, O., Lee, R. K., Scherer, A., Yariv, A., O'Brien, J. D., Dapkus, P. D. & Kim, I. (1999). Two-dimensional photonic band-gap defect mode laser, *Science* 284(11): 1819–1821.
- Peterson, A. F., Ray, S. L. & Mittra, R. (1998). *Computational Methods for Electromagnetics*, IEEE Press, New York.
- Ryu, H.-Y., Kim, S.-H., Park, H.-G., Hwang, J.-K. & Lee, Y.-H. (2002). Square-lattice photonic band-gap single-cell laser operating in the lowest-order whispering gallery mode, *Applied Physics Letters* 80(21): 3883–3885.
- Sadiku, M. N. O. (2000). *Numerical Techniques in Electromagnetics*, CRC Press, Boca Raton.
- Sakoda, K. (2001). *Optical Properties of Photonic Crystals*, Springer, Germany.

- Schawlow, A. L. & Townes, C. H. (1958). Infrared and optical masers, *Physical Review* 112(6): 1940–1949.
- Shih, M. H., Kim, W. J., Wuang, W., Cao, J. R., Yukawa, H., Choi, S. J., O'Brien, J. D. & Marshall, W. K. (2004). Two-dimensional photonic crystal machzehnder interferometers, *Applied Physics Letters* 84(4): 460–462.
- Shih, M. H., Kuang, W., Mock, A., Bagheri, M., Hwang, E. H., O'Brien, J. D. & Dapkus, P. D. (2006). High-quality-factor photonic crystal heterostructure laser, *Applied Physics Letters* 89: 101104–1–101104–3.
- Shih, M. H., Kuang, W., Yang, T., Bagheri, M., Wei, Z.-J., Choi, S.-J., Lu, L., O'Brien, J. D. & Dapkus, P. D. (2006). Experimental characterization of the optical loss of sapphire-bonded photonic crystal laser cavities, *Photonics Technology Letters* 18(3): 535–537.
- Shih, M. H., Mock, A., Hwang, E. H., Kuang, W., O'Brien, J. D. & Dapkus, P. D. (2006). Photonic crystal heterostructure laser with lattice-shifted cavity, *Conference on Lasers and Electro-Optics Technical Digest*, Baltimore, MD, p. paper CMKK3.
- Smith, C. L. C., Wu, D. K. C., Lee, M. W., Monat, C., Tomljenovic-Hanic, S., Grillet, C., Eggleton, B. J., Freeman, D., Ruan, Y., Madden, S., Luther-Davies, B., Giessen, H. & Lee, Y.-H. (2007). Microfluidic photonic crystal double heterostructures, *Applied Physics Letters* 91: 121103–1–121103–3.
- Soda, H., Iga, K., Kitahara, C. & Suematsu, Y. (1979). Gainasp/inp surface emitting injection lasers, *Japan Journal of Applied Physics* 18(12): 2329–2330.
- Song, B.-S., Asano, T. & Noda, S. (2007). Heterostructures in two-dimensional photonic-crystal slabs and their application to nanocavities, *Journal of Physics D* 40: 2629–2634.
- Song, B.-S., Noda, S., Asano, T. & Akahane, Y. (2005). Ultra-high-Q photonic double heterostructure nanocavity, *Nature Materials* 4: 207–210.
- Taflove, A. & Hagness, S. C. (2000). *Computational electrodynamics*, Artech House, Massachusetts.
- Takahashi, Y., Hagino, H., Yoshinori, T., Song, B.-S., Asano, T. & Noda, S. (2007). High-Q nanocavity with a 2-ns photon lifetime, *Optics Express* 15(25): 17206–17213.
- Tanabe, T., Notomi, M., Kuramochi, E., Shinya, A. & Taniyama, H. (2007). Trapping and delaying photons for one nanosecond in an ultrasmall high-Q photonic-crystal nanocavity, *Nature Photonics* 1: 49–52.
- Tanaka, Y., Asano, T. & Noda, S. (2008). Design of photonic crystal nanocavity with Q-factor of $\sim 10^9$, *Journal of Lightwave Technology* 26(11): 1532–1539.
- Tomljenovic-Hanic, S., Steel, M. J., de Sterke, C. M. & Moss, D. J. (2007). High-Q cavities in photosensitive photonic crystals, *Optics Letters* 32(5): 542–544.
- Vlasov, Y. A., O'Boyle, M., Hamann, H. F. & McNab, S. J. (2005). Active control of slow light on a chip with photonic crystal waveguides, *Nature* 438: 65–69.
- Yablonovitch, E., Gmitter, T. J. & Leung, K. M. (1991). Photonic band structure: The face-centered-cubic case employing nonspherical atoms, *Physical Review Letters* 67(17): 2295–2298.
- Yang, T., Lipson, S., Mock, A., O'Brien, J. D. & Deppe, D. G. (2007). Edge-emitting photonic crystal double-heterostructure nanocavity lasers with inas quantum dot material, *Optics Letters* 32(9): 1153–1155.

- Yoshie, T., Scherer, A., Hendrickson, J., Khitrova, G., Gibbs, H. M., Rupper, G., Ell, C., Shchekin, O. B. & Deppe, D. G. (2004). Vacuum rabi splitting with a single quantum dot in a photonic crystal nanocavity, *Nature* 432: 200–203.
- Zhang, Z. & Qiu, M. (2004). Small-volume waveguide-section high Q microcavities in 2d photonic crystal slabs, *Optics Express* 12(17): 3988–3995.